Journal of Manufacturing Processes 139 (2025) 1–11

Contents lists available at ScienceDirect

Journal of Manufacturing Processes

journal homepage: www.elsevier.com/locate/manpro

Incorporation of acrylated cellulose nanocrystals into photocurable resin for high-fidelity printing of transparent 3D structures

Junsik Choi [a,1], Deepika Thakur [a,1], Jinhong Min [c], Jiho Lee [c], Hoon Kim [b,c,*], Jinho Hyun [a,*]

[a] Department of Agriculture, Forestry and Bioresources, Seoul National University, Seoul 08826, Republic of Korea
[b] Research Institute of Agriculture and Life Sciences, Seoul National University, Seoul 08826, Republic of Korea
[c] Graphy Inc., Graphy R&D Center, Seoul 08501, Republic of Korea

ARTICLE INFO

Keywords:
Cellulose nanocrystals
Acrylated CNC
UV-curable resin
Digital light processing
3D printing
Shape memory
Bioengineering

ABSTRACT

The incorporation of cellulose nanocrystals (CNCs) into trimethylolpropane formal acrylate (CTFA) ink for digital light processing (DLP) 3D printing has been found to increase light scattering, which subsequently reduces the mechanical properties of printed structures. In this study, acrylated cellulose nanocrystals (A-CNCs) were synthesized by treating sulfonated CNCs with methacrylic acid and were successfully integrated into a UV-curable resin for DLP 3D printing. The effect of ultrasonication on A-CNC dispersion within the resin was assessed by measuring the change in the transmittance of suspensions. The composite resin ink containing A-CNCs retained transparency, and the resulting printed structures demonstrated significant mechanical reinforcement even at low A-CNC concentrations. This improvement is attributed to the high colloidal stability of A-CNCs within the ink. Furthermore, the suitability of the resin for 3D printing was confirmed through the examination of the morphologies of the printed structures. Moreover, the structures printed using A-CNC/CTFA exhibited shape memory behavior in response to thermal stimuli, affirming the potential of the composite resin in bioengineering applications.

1. Introduction

Additive manufacturing, which allows the design and direct printing of three-dimensional (3D) objects, has significantly promoted industrial and advanced material research. Notably, the rapid advancement of 3D printing technology has had a profound impact across various fields in healthcare, including surgery, bioengineering, orthopedics, and dentistry [1–10]. Among the diverse 3D printing techniques, UV-curable 3D printing is distinguished by its precision and capacity to create intricate geometries with fine details. This method employs photopolymer resins that solidify upon exposure to ultraviolet (UV) light, making it highly suitable for applications demanding high-resolution fabrication [11–13].

A key advantage of UV-curable 3D printing is its ability to easily produce transparent 3D structures. These transparent structures are valuable in numerous medical applications such as medical devices, implants, and orthopedic apparatuses [14–16]. Transparency in these structures is particularly important for real-time monitoring of processes and clinical outcomes as well as for visual inspections to assess security integrity. This capability is essential for accurate diagnosis and treatment planning. Trimethylolpropane formal acrylate (CTFA) is particularly attractive in biomedical engineering owing to its clarity and shape memory properties [17]. To achieve transparent structures with CTFA, the ink must satisfy specific criteria, including optical clarity, uniformity, and compatibility with UV-curable resins [18]. Optical clarity ensures that the structure appears transparent, while uniformity is crucial for maintaining consistent physical and mechanical properties throughout the material. Furthermore, compatibility with UV-curable resins is vital to ensure appropriate curing of the ink during the printing process, enabling the formation of the desired structures [19,20].

However, transparent structures face several challenges such as low crystallinity, reduced mechanical strength, and potential degradation of

Abbreviations: CNCs, cellulose nanocrystals; A-CNCs, acrylated cellulose nanocrystals; S-CNCs, sulfonated cellulose nanocrystals; CTFA, trimethylolpropane formal acrylate; DLP, digital light processing; UV, ultraviolet; TEMPO, 2,2,6,6-tetramethylpiperidine-1-oxyl; MMA, methacrylic acid; FTIR, Fourier-transform infrared; UTM, universal testing machine.

* Corresponding authors.
E-mail addresses: c12o2cl4@snu.ac.kr (H. Kim), jhyun@snu.ac.kr (J. Hyun).
[1] These authors contributed equally.

https://doi.org/10.1016/j.jmapro.2025.02.023
Received 2 December 2024; Received in revised form 16 January 2025; Accepted 11 February 2025
Available online 13 February 2025

printing precision. Reduced mechanical strength may diminish the durability and practicality of printed structures, while a decrease in printing precision hinders the accurate reproduction of complex geometries. To overcome these limitations, it is essential to incorporate biocompatible nanomaterials that can concurrently achieve high transparency and mechanical strength.

Nanoparticles can enhance the mechanical strength of inks while preserving transparency; however, optimizing the interaction between nanoparticles and resins is critical. Surface treatment of nanoparticles may be required to ensure colloidal stability and uniform dispersion [21]. In this study, cellulose nanocrystals (CNCs), derived from natural cellulose, were selected as the reinforcement material because of their large surface area, high aspect ratio, exceptional mechanical strength, and biodegradability [22–24]. Nevertheless, the surface charge of CNCs is different from that of resins, necessitating chemical surface modification. Acrylation of CNCs improves their compatibility with UV-curable resins, facilitating better dispersion and stronger interaction within the polymer matrix [18,23,25]. The CNC modified with acrylation was used to enhance the dispersion of nanocrystal fillers in methacrylic-based resins using Stereolithography (SLA) printing [26]. The study also highlights the effectiveness of adding A-CNC for increasing the dielectric constant and easy curing for printing complex structures such as tooth sockets and flowers with good mechanical properties. However, poor transparency and poor choice of resin lead to the yellow color of printed structures which cannot be utilized for biomedical applications. Feng et al. mentioned that adding the CNCs into acrylate resin matrix for SLA printing also enhances the overall dissipation of stresses in deformed matrices and improve the mechanical properties of printed composites to some extent [27]. Similarly, CNC added as a reinforcement matrix improved the mechanical properties of printed structures in DLP printing with poly(ethylene glycol) diacrylate and glycerol 1,3-diglycerolate diacrylate matrix [28]. However, due to poor compatibility of CNC with acrylate resin matrix and its hydrophilic functional groups, the composite resin needed to be continuously stirred before use in both SLA and DLP printing, which can be a very tedious process. Also, due to poor dispersibility, it becomes very challenging to overcome the decrease in mechanical properties. To avoid this, CNC grafted with poly(methyl methacrylate) was used and the compatibility between surface-modified acrylated CNC and resin matrix have been improved [29]. The incorporation of A-CNC is crucial for the improvement of mechanical properties of 3D printed structures due to interfacial compatibility, dispersibility and compatibility with CTFA resin matrix.

In this study, we employed acrylated CNCs (A-CNCs) as nanofillers within a UV-curable CTFA resin to improve compatibility and dispersibility *via* surface functional groups. The surface acrylation of CNCs reduced the interfacial tension between CNCs and CTFA resin, and acryl functional groups at the surface would interact with acryl groups in CTFA resin forming binding sites. While hydrophilic functional groups of unmodified CNCs alone could not achieve the proper compatibility, acrylation effectively prevented agglomeration in the CTFA ink, even with prolonged ultrasonication. This modification also enhanced the transparency of the composite ink by promoting uniform dispersion, which is essential for UV-curing. Moreover, acrylation significantly improved the mechanical properties. The incorporation of A-CNC is crucial for the improvement of mechanical properties of 3D printed structures due to interfacial compatibility, dispersibility and compatibility with CTFA resin matrix. It distinctly targets applications in orthodontics and biliary stents, concentrating on their specific behavioral requirements. We focus on 3D printing outputs at the low concentration of A-CNCs examining in detail the shape memory characteristics, mechanical properties, and final print quality using DLP. To the best of our knowledge, this is the first study to highlight the incorporation of surface-modified CNCs into CTFA-based UV-curable inks with such a specific emphasis on these medical applications and the corresponding 3D printing behaviors.

2. Experimental section

2.1. Preparation of acrylated cellulose nanocrystals (A-CNCs)

Sulfuric-acid-hydrolyzed CNC (S-CNC) powder (Celluforce, Montreal, Canada) was used to prepare A-CNCs. First, a homogeneous aqueous suspension of S-CNCs (1 wt%) was prepared by magnetic stirring at 200 rpm for 30 min. Then, 0.1 g of potassium persulfate and 1 g of 2,2,6,6-tetramethylpiperidine-1-oxyl (TEMPO) were mixed with the S-CNC suspension in a three-neck round bottom flask. Next, 10 mL of methacrylic acid (MAA, Junsei Chemical Co. Ltd., Japan) was added dropwise to the solution at 70 °C using a syringe pump, and the solution was stirred at 600 rpm for 2, 4, and 6 h. The solution was cooled to room temperature and ultracentrifuged at 8000 rpm. The supernatant was removed to isolate A-CNCs, which were then resuspended in distilled water. The purification process was repeated three times. The resulting gel-like solution was freeze-dried for 3 days, and dried A-CNCs were stored at room temperature until use.

2.2. Preparation of composite resin ink

Here, 1 wt% of phenylbis(2,4,6-trimethylbenzoyl)phosphine oxide (Irgacure 819, BASF, Ludwigshafen, Germany) was added to CTFA (Miwon Specialty Chemical Co., Ltd., Yongin-si, Republic of Korea) and sonicated using an ultrasonic dispersing machine (VCX-130, SONICS, United States) with a 13 mm diameter solid probe (630–0560, SONICS, United States) at 70 % amplitude for 1 min to ensure the complete dispersion of the initiator. After the photoinitiator was dispersed in CTFA, the mixture was cooled before adding A-CNCs at 0.05, 0.1, and 0.2 wt%. The composite suspension was mixed using a vortex mixer (SI-0246 A Vortex-Genie2, Scientific Industries Inc., United States) for 1 min and treated by ultrasonication at 70 % amplitude for various durations (0, 30, 60, and 120 s). During sonication, the bottle containing the ink was placed in an ice bath to prevent overheating.

2.3. Printability of composite ink

The 3D CAD design models were created using Rhinoceros 5.0 (Robert McNeel & Associates, United States) and sliced with the Anycubic Photon Workshop software (Anycubic, Shenzhen, China). The printing slice parameters were set with a layer thickness of 100 μm, an exposure time of 3 s, and an off time of 1 s between each slice. 3D printing was performed using an LCD 3D printer (Photon Mono 2, Anycubic, Shenzhen, China).

2.4. Chemical structure of A-CNCs

Fourier-transform infrared (FTIR) spectroscopy (Nicolet iS5, Thermo Scientific, Waltham, MA, United States) was conducted to analyze the chemical structure of S-CNCs after grafting. FTIR spectroscopy was performed in the wavenumber range of 4000–500 cm^{-1} at a resolution of 4 cm^{-1} and a scan number of 32. The 5 replicates were used for each samples for the analysis of FT-IR.

2.5. Surface charge of A-CNCs

The surface charge of the S-CNC and A-CNC suspensions, prepared at 2, 4, and 6 h, was analyzed using a Malvern Zetasizer (Nano ZS90, Malvern Panalytical, Malvern, United Kingdom). The 5 replicates were used for each samples for the analysis of zeta potential. The sample suspension was prepared at 0.1 wt% in deionized water followed by sonicated for 2 min. No control samples were used during analysis.

2.6. Dispersibility of composite suspension

The hydrodynamic diameter of the composite suspension was

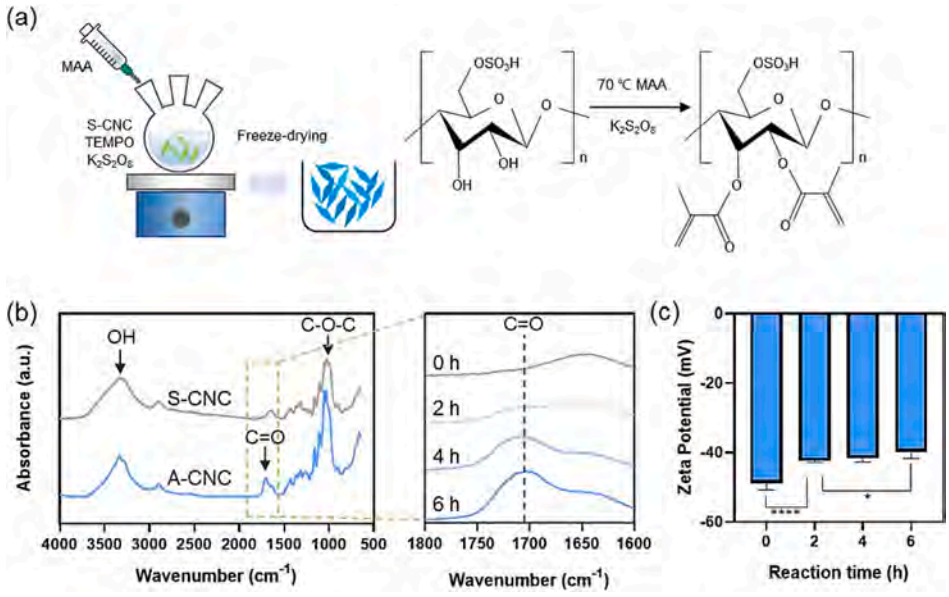

Fig. 1. (a) Illustration of the acrylation process of S-CNCs. (b) FTIR spectra of S-CNCs and A-CNCs at different reaction times. (c) Zeta potential of A-CNCs at various reaction times.

measured using a zetasizer (ZSU 3150, Malvern Instruments, Malvern, UK). Each sample was diluted 10-fold with isopropyl alcohol (99.8 %, SAMCHUN, Korea). The transmittance of the composite suspensions was measured using a UV–visible light spectrophotometer (Optizen POP, Mecasys Co., Ltd., Republic of Korea) in the spectrum mode in the wavelength range of 380–420 nm and in the photometric mode at 405 nm. The change in the transmittance of the composite resin was measured at 405 nm in the kinetic mode for 60 min with a time interval of 5 mins. The 3 replicates were used for each samples for the analysis of hydrodynamic diameter and UV–visible light spectroscopy.

2.7. Turbidity of suspensions

To assess the colloidal stability of the composite inks during the extended 3D printing process, the turbidity of the A-CNC/CTFA composite resin was measured using the Tyndall effect. A commercially available laser pointer with a deep-red laser diode near 650 nm was used. A 20 mL vial was filled with 10 mL of the composite resin. The laser was aimed at a height of 1 cm from the bottom of the vial, and photographs were taken in a dark environment. After the suspension remained static for 1 h, another set of photographs was taken.

2.8. Rheological properties

The rheological properties of the composite resin were evaluated using a rotational rheometer (MCR 702e, Anton Paar, Graz, Austria) equipped with a parallel plate geometry. Measurements were performed under oscillatory mode with a strain amplitude of 1 % and a frequency of 1 Hz. The samples were exposed to ultraviolet (UV) light during testing using a UV source (CTLAB ctc4ene4-b63f, 500 W) set at an intensity of 10.3 mW/cm^2 (5 % of maximum output). The UV exposure was applied continuously for 300 s while monitoring the resin's viscoelastic properties. The 3 replicates were used for each samples for the analysis of rheological properties.

2.9. Mechanical properties

The mechanical strength of the printed resin was measured using a universal testing machine (UTM, GB/LRX Plus, Lloyd, West Sussex, United Kingdom) fitted with a 500 N load cell. Uniaxial tensile tests were performed according to the ASTM D412 specification for elastomers. Tests were conducted at a speed of 0.5 mm/s. Tensile strength and strain at break were determined as the stress and strain at specimen breakage, respectively. The modulus was defined as the initial slope of the stress–strain curve. The 3 replicates were used for each samples for the analysis of mechanical properties.

To perform Weibull analysis, 15 tensile tests were conducted for the CTFA/A-CNC and CTFA/S-CNC composites at various concentrations (0.05, 0.1, and 0.2 wt%). The survival probability as a function of ultimate tensile stress was fitted to an asymmetric sigmoidal curve. The fitting and analysis were performed using the nonlinear analysis function of the GraphPad Prism software.

2.10. Thermally induced shape memory analysis

The thermally induced shape memory behavior was evaluated using the 3D-printed samples with CTFA and A-CNC/CTFA resin. The printed samples were initially softened in a water bath maintained at 85 °C for 30 s. The deformed samples were quickly fixed by transferring them to an ice water bath at 4 °C for 30 s. The samples were then immersed in a water bath at 40 °C to observe shape recovery behavior. The sample replicates were used for the measurement were 3 for each sample.

A fold-deploy test was conducted to quantitatively assess the shape memory performance. Rectangular samples with dimensions of 50 mm in length, 20 mm in width, and 2 mm in thickness were 3D printed. These samples were folded into a U-shape, with the two parallel blades in a water bath at 85 °C for 30 s. After deformation, the shapes were fixed in an ice water bath at 4 °C for 30 s. The U-shaped specimens were then immersed in water at 40 °C for 3 min, during which the angle between the blades (θ_f) was measured. The shape recovery ratio (R_r) was calculated using the following Eq. (1):

$$R_r = \frac{\theta_f}{180^\circ} \times 100\% \quad (1)$$

2.11. Cell viability

The cell-viability assay was performed following the ISO-10993-5 standard on NIH-3 T3 fibroblast cells. Cells were cultured in DMEM media (Sigma Aldrich, St. Louis, United States) containing 8 % fetal bovine serum (Thermo Fisher Scientific, Waltham, United States) and 2

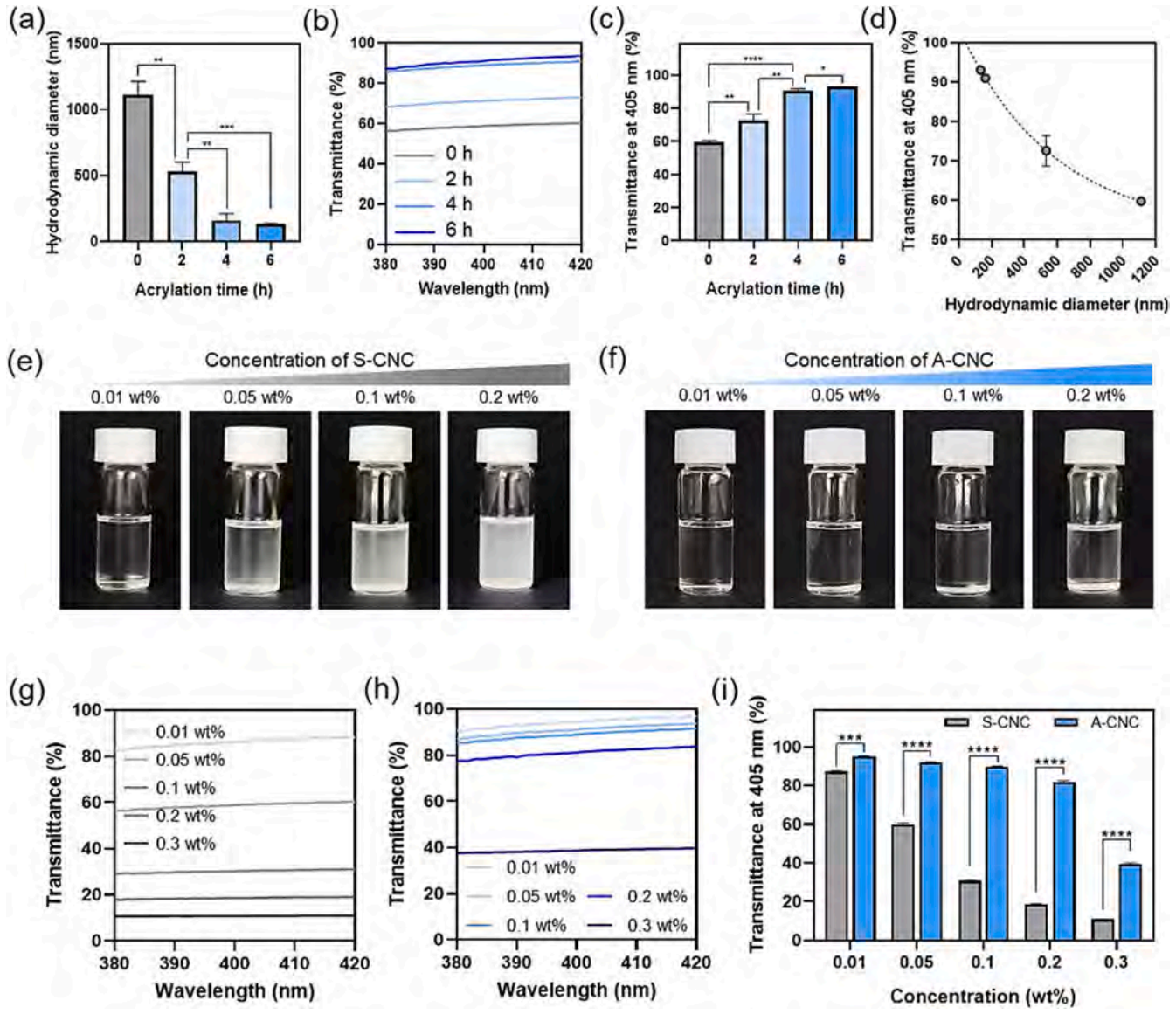

Fig. 2. Dispersibility of A-CNCs in the CTFA resin. (a) Transmittance spectrum and (b) transmittance at 405 nm of the A-CNC/CTFA composite resin as a function of acrylation reaction time. (c) Hydrodynamic diameter of the A-CNC resin at different acrylation reaction times. Optical images of the composite resins with various concentrations of (d) S-CNCs and (e) A-CNCs. Transmittance of the (f) S-CNC/CTFA and (g) A-CNC/CTFA composite resins at different concentrations. (h) Transmittance at 405 nm of the composite resin with various S-CNC and A-CNC concentrations. Ultrasonication time was 120 s.

% penicillin/streptomycin (Sigma Aldrich, St. Louis, United States) at 37 °C and 5 % CO_2. The extract solution of UV-cured CTFA and composite sheets in the incubation media was used to assess cell viability. Cells (3.5×10^3 cells/well) were cultured with 100 μL of the extract solution in 96-well plates for 24 h at 37 °C and 5 % CO_2. The MTT assay was conducted using standard protocols. Absorbance was measured at 570 nm using an ELISA reader (Varioskan ALF, Thermo Fisher Scientific, Waltham, United States). The 3 replicates were used for each samples for the analysis of cell viability.

2.12. Cell adhesion

For cell adhesion analysis, wells with an inner diameter of 10 mm were printed using the composite inks consisting of CTFA and 0.1 wt% of S-CNCs and A-CNCs by DLP. The 3×10^4 cells were seeded into each well and incubated at 37 °C and 5 % CO_2 for 24 h. The cells were washed with PBS and observed using a fluorescence microscope (Celena S Digital Imaging System, Korea) after staining with 1 mM CytoFluor-AM/DMSO and 1.5 mM propidium iodide (MAX-View, Korea) for 20 min. The 3 replicates were used for each samples for the analysis of cell adhesion.

3. Results and discussion

The surface of S-CNCs was modified with acryl functional groups using a TEMPO-assisted reaction (Fig. 1a). S-CNCs, crystalline particles of cellulose typically extracted *via* an acid-hydrolysis method, contain hydroxyl and sulfated functional groups on its surface, making it susceptible to chemical modification. S-CNCs are known for their high mechanical strength, which makes it suitable as a nanofiller in composite materials. However, its hydrophilic nature limits its compatibility with hydrophobic resins like CTFA. CTFA, being an acrylated resin with high hydrophobicity, leads to phase separation and aggregation when mixed with S-CNCs. This aggregation reduces colloidal stability, increases light scattering, and results in a diffused curing process, which significantly lowers the printing fidelity.

To address these issues, the surface of S-CNCs was modified to form A-CNCs by acrylating its functional groups. This modification improves the chemical affinity between A-CNCs and the acryl groups of CTFA,

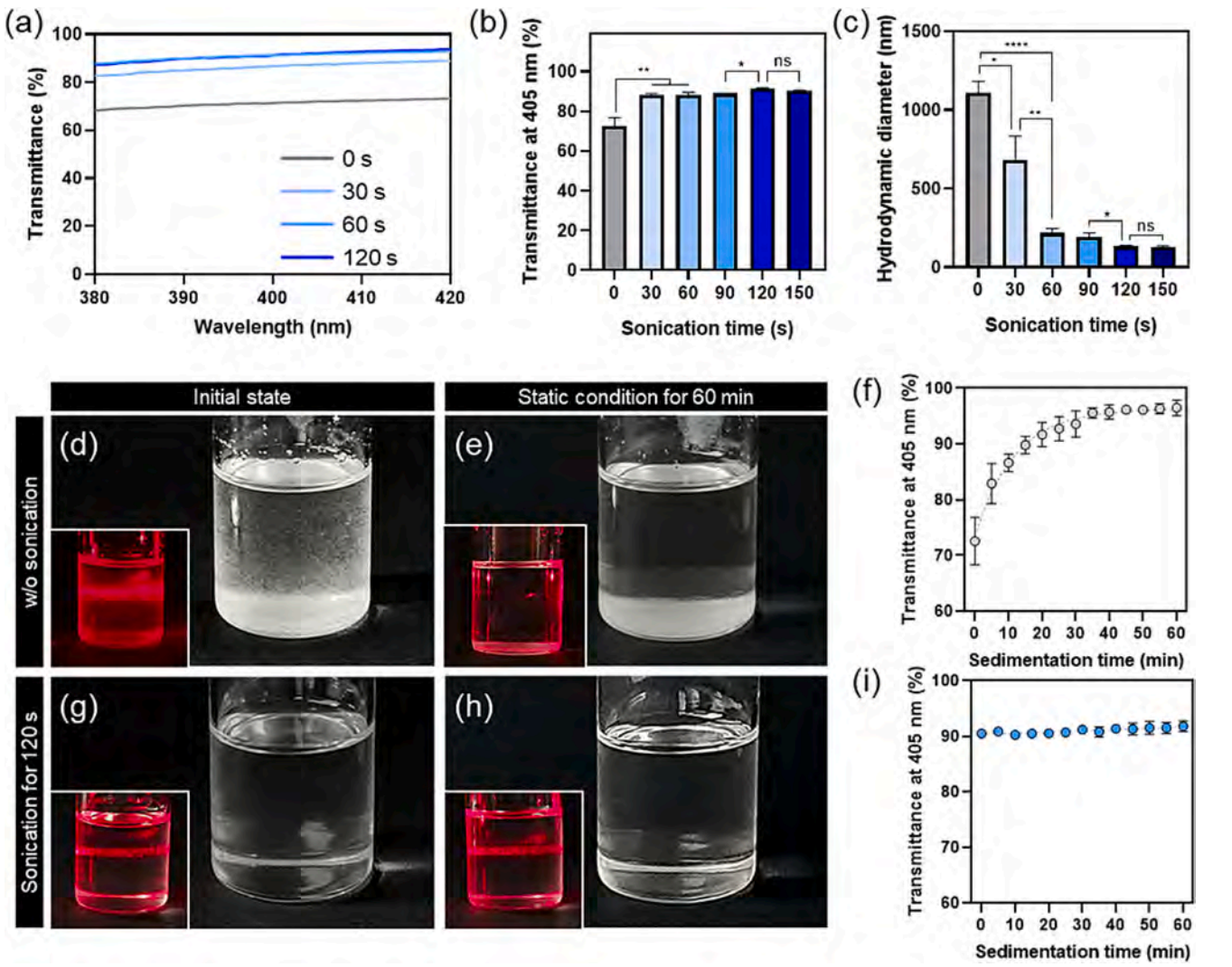

Fig. 3. (a) Transmittance spectrum of the A-CNC/CTFA resin at various sonication times. (b) Transmittance at 405 nm for the A-CNC/CTFA resin at different sonication times. (c) Hydrodynamic diameter of A-CNCs in the composite resin at various sonication times. (d) Initial state of the nonsonicated composite ink. (e) Composite ink after 60 min without sonication. (f) Initial state of the composite resin sonicated for 120 s. (g) Composite resin after 60 min upon 120 s sonication. (h) Transparency change over time for the nonsonicated sample. (i) Transparency changes over time for the sample sonicated for 120 s. A-CNC concentration: 0.1 wt%.

thereby enhancing the colloidal stability of the composite ink through increased miscibility between A-CNCs and CTFA. MAA was used as the input monomer, with $K_2S_2O_8$ acting as the catalyst and TEMPO serving as the crosslinking inhibitor at 70 °C. After the reaction, the final products were centrifuged, obtained as powder, and freeze-dried.

The FTIR spectra confirmed the successful acrylation of S-CNCs (Fig. 1b). The broad peak at 3334 cm^{-1} corresponds to the stretching vibrations of hydroxyl (-OH) groups, while the peak at 2900 cm^{-1} is ascribed to C—H stretching vibrations. Additionally, peaks attributed to the C-O-C stretching vibrations from the cellulose backbone were observed. After grafting with MAA, a new peak emerged at 1704 cm^{-1} due to C═O stretching vibrations, confirming the successful grafting onto S-CNCs. The appearance of this peak was consistent across different reaction times of 2, 4, and 6 h, highlighting the importance of reaction time in realizing appropriate chemical grafting.

Zeta potential measurements further supported the successful modification of S-CNCs into A-CNCs. The zeta potential values for S-CNCs and A-CNCs at 2, 4, and 6 h were − 48.92 ± 1.38, −42.43 ± 0.35, −41.7 ± 0.92, and − 39.88 ± 1.30, respectively (Fig. 1c). The high negative zeta potential values of A-CNCs, close to those of S-CNCs, indicate that the modification primarily occurred at the C2 and C3 positions of the cellulose structure rather than at the C6 sulfate groups.

The hydrodynamic diameter of A-CNCs in the CTFA resin decreased with increasing acrylation reaction time (Fig. 2a). Although S-CNCs exhibited micrometer-scale agglomeration within the CTFA resin, highly acrylated A-CNCs was dispersed in much smaller sizes under the same dispersion conditions. This reduction in the hydrodynamic diameter reflects improved dispersion and uniform distribution of A-CNCs in the resin matrix, which are critical for enhancing printability and mechanical properties.

The transmittance spectrum of the A-CNC/CTFA composite resin demonstrated a notable improvement in transparency within the 380–420 nm range as the acrylation reaction time increased, as shown in Fig. 2b. Specifically, the photoinitiation of the composite resin occurred at 405 nm, and the transparency of the CTFA composite resin containing S-CNCs was approximately 60 %, primarily owing to high turbidity. This turbidity is attributed to light scattering at the interfaces of the immiscible S-CNCs within the CTFA resin. As the acrylation reaction time increased, the transparency progressively improved, reaching up to 93 % (Fig. 2c). This enhancement indicates more uniform dispersion and improved compatibility of A-CNCs with the resin matrix.

A correlation analysis was conducted to investigate the relationship between hydrodynamic diameter and transparency of the composite

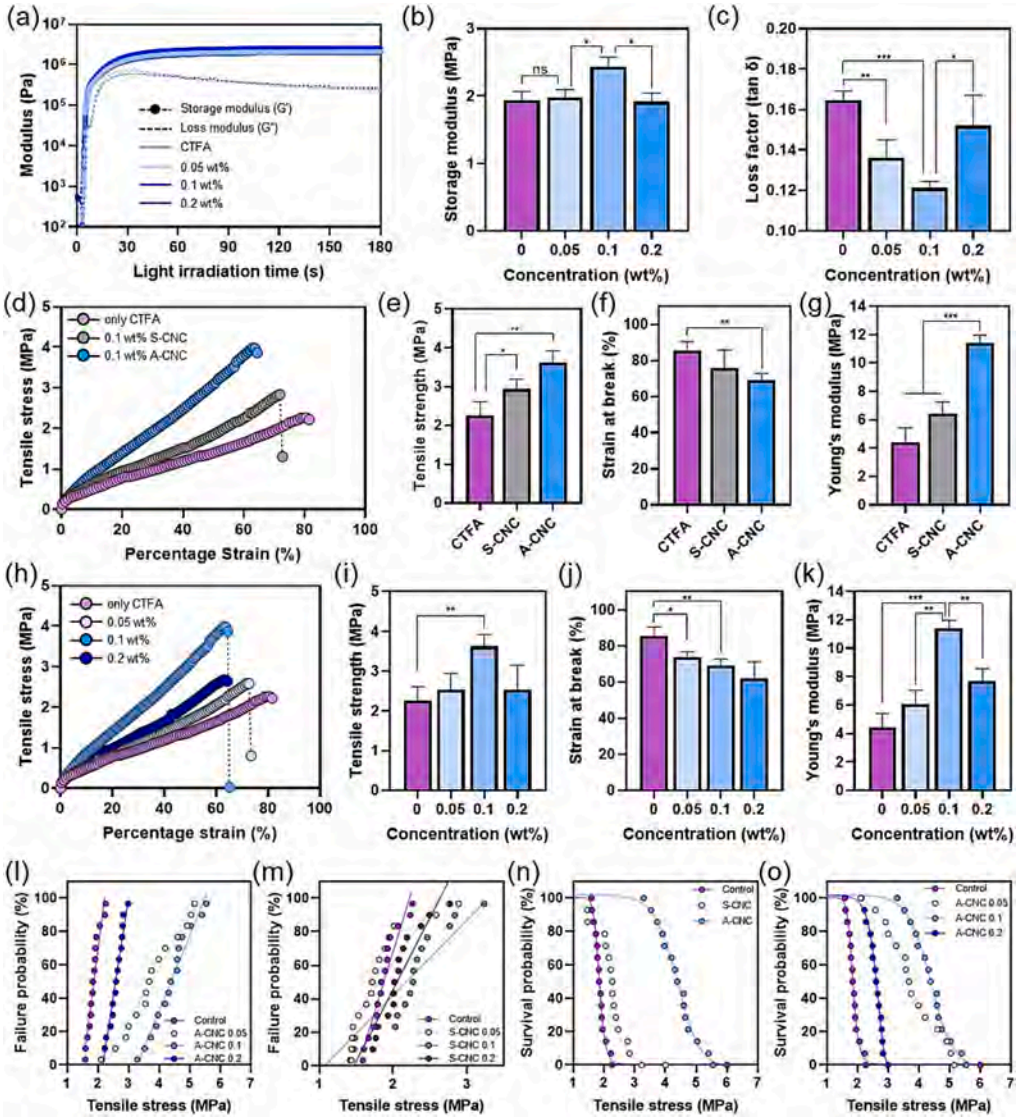

Fig. 4. (a) Changes in the moduli during *in situ* photocuring at various concentrations of A-CNCs (0, 0.05, 0.1, and 0.2 wt%). (b) Enhancement in the storage modulus (G') with the addition of A-CNCs. (c) Variation in the loss factor (tan δ) at different A-CNC concentrations. (d) Stress–strain curve for the composite resin with 0.1 wt% A-CNCs and S-CNCs. Comparison of (e) tensile strength, (f) strain at break, and (g) Young's modulus between the A-CNC and S-CNC composite resins. (h) Stress–strain curve for the composite resin with varying concentrations of A-CNCs (0, 0.05, 0.1, and 0.2 wt%). Comparison of (i) tensile strength, (j) strain at break, and (k) Young's modulus at different A-CNC concentrations. (l) Weibull survival probability based on tensile strength for 0.1 wt% A-CNCs and S-CNCs in CTFA. (m) Concentration of A-CNCs in CTFA.

resin inks. The results showed that as the hydrodynamic diameter of A-CNCs decreased, the transparency of the resin increased, indicating improved dispersion and reduced light scattering. This trend highlights the critical role of particle size in achieving optimal optical clarity, as shown in Figure 2d.

Fig. 2e and f present the optical images of the composite resins containing various concentrations of S-CNCs and A-CNCs in CTFA, respectively. The transparency of the S-CNC-containing resin decreased rapidly, resulting in an opaque appearance at concentrations above 0.1 wt%. In contrast, A-CNCs maintained relatively high transparency even at concentrations exceeding 0.1 wt%, underscoring its superior dispersibility, a result of surface acrylation. The transmittance spectra of the S-CNC/CTFA and A-CNC/CTFA composite resins further confirmed a significant reduction in the transparency of S-CNC/CTFA (Fig. 2g and h). Effective dispersion of A-CNCs in the CTFA resin was achieved through sonication prior to DLP printing due to their high compatibility. At A-CNC concentrations above 0.1 wt%, the increased particle number primarily caused increased light scattering and a subsequent reduction in transparency. Notably, both S-CNC and A-CNC faced challenges in achieving high transparency at concentrations exceeding 0.2 wt% becoming too opaque for UV curing. However, the decrease in the transparency of A-CNCs was significantly less, highlighting the improved compatibility and dispersion of A-CNCs within the resin matrix, even at higher concentrations (Fig. 2i).

Ultrasonication was employed to enhance the dispersion of A-CNCs within the CTFA resin. The transparency of the composite resin ink varied with different sonication treatment times (Fig. 3). With ultrasonication time, the transparency of the composite resin ink increased, indicating the improved dispersion of A-CNCs within the resin matrix (Fig. 3a and b). This enhancement in transparency suggests that A-CNCs were more evenly distributed, reducing light scattering and enhancing optical clarity. The hydrodynamic diameter of the dispersed A-CNCs decreased as sonication time increased, implying that sonication caused the separation of aggregated A-CNCs and prevention of their re-aggregation (Fig. 3c). However, no significant improvement in

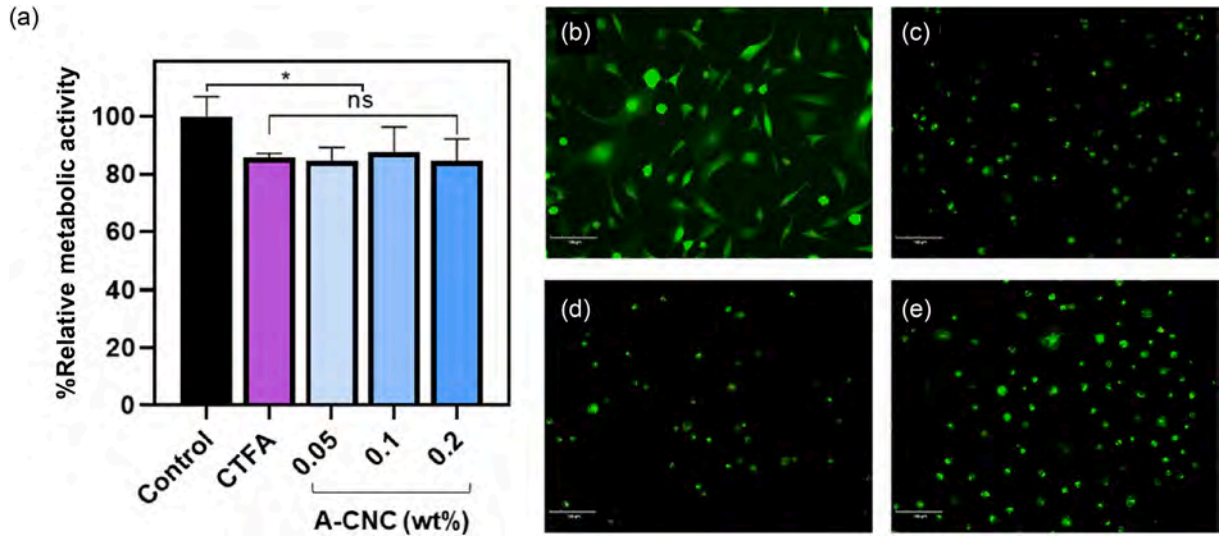

Fig. 5. (a) Relative metabolic activity of the NIH3T3 fibroblast cells. Eluate was prepared after incubating the specimen in the incubation medium for 24 h. Fluorescent images of the cells seeded on (b) the control, (c) CTFA, (d) CTFA with 0.1 % S-CNC, and (e) CTFA with 0.1 % A-CNC sheets. The cells were incubated for 1 day.

transparency or decrease in hydrodynamic diameter was observed beyond 120 s of ultrasonication indicating an optimal processing condition with the dispersion efficiency.

Maintaining colloidal stability in composite inks is crucial for 3D printing processes, which typically require extended timeframes to complete. The colloidal stability of the dispersed A-CNC/CTFA composite resin was investigated under static conditions over 30 min. Fig. 3d shows the nonsonicated composite resin ink at the initial stage. The adjacent image of the laser beam passing through the resin illustrates the Tyndall effect, confirming the formation of a colloid in the initial state. The Tyndall effect, the scattering of light by particles in a colloid, is visible as a beam of light passing through the mixture and serves as an indicator of colloidal stability.

However, the nonsonicated A-CNC/CTFA composite resin exhibited the sedimentation of A-CNCs after 30 min of storage, leading to the disappearance of the Tyndall effect (Fig. 3e). The increase in transmittance over 60 min of storage time resulted from the sedimentation of particles, because the detection beam path was positioned in the middle of the cuvette (Fig. 3f). In contrast, Fig. 3g shows the composite resin ink sonicated for 120 s. The persistent Tyndall effect suggested that A-CNCs were well dispersed in the CTFA resin. The colloidal stability was maintained over the 30 min storage period, with the Tyndall effect remaining consistent (Fig. 3h) and the transmittance at 405 nm remaining high (Fig. 3i). The transparency of the sonicated composite resin inks was preserved over time, indicating stable dispersion without significant sedimentation. The composite resin ink with A-CNC showed the high colloidal stability at room temperature for a long period due to high compatibility. No significant aggregation of A-CNCs in the composite ink was observed after the storage for at least one week. In the report, we focused on the reliable printing within 60 min to manufacture the small size of medical devices. The A-CNC/CTFA resin ink maintained colloidal stability without sedimentation for 60 min. It ensured suitability for DLP printing processes which typically completed within this timeframe.

These observations confirm that ultrasonication effectively improves the dispersion of A-CNCs in the CTFA resin, maintaining colloidal stability and preventing sedimentation.

Furthermore, the modulus of the composite resin ink was monitored *in situ* during the photocuring process at different concentrations of A-CNCs (Fig. 4a). For all concentrations, a significant change in modulus occurred within 30 s of light exposure, indicating rapid photopolymerization. This rapid increase in modulus suggests efficient crosslinking in the presence of A-CNCs, without hindering the photopolymerization process. The storage modulus (G′), which represents the elastic behavior of the material, showed a marked increase with the addition of A-CNCs. The most significant improvement was observed at 0.1 wt% A-CNCs in the composite resin (Fig. 4b), where storage modulus showed a statistically significant difference ($p < 0.05$) compared to both 0.05 wt% and 0.2 wt% conditions. The increase in G′ signifies enhanced stiffness and mechanical stability of the composite material, making it suitable for applications that demand robust mechanical properties. The loss factor (tan δ), defined as the ratio of the loss modulus (G″) to G′, is a crucial parameter for understanding the viscoelastic behavior of materials. A lower tan δ indicates more solid-like behavior and reduced dissipation of energy as heat. At 0.1 wt% A-CNCs, the loss factor was the lowest, suggesting that the material at this concentration achieved the highest degree of solidification and structural integrity (Fig. 4c). This optimal concentration strikes a balance between sufficient crosslinking and mechanical reinforcement, contributing to the overall enhancement of the composite material.

The stress–strain curve (Fig. 4d) illustrates the tensile properties of the composite resins containing 0.1 wt% A-CNCs and S-CNCs. Both composites exhibited improved tensile strength in relation to those of the samples prepared with only CTFA, indicating a reinforcement effect induced by the CNCs. However, the A-CNC composite demonstrated a stronger reinforcing effect on tensile strength owing to its higher miscibility with the resin.

The A-CNC composite exhibited higher tensile strength than the S-CNC composite (Fig. 4e), which can be attributed to more effective stress transfer and stronger load-bearing capacity within the matrix. The strain at break was lower for both A-CNC and S-CNC composites than for the sample with CTFA alone (Fig. 4f), indicating increased brittleness as a result of reinforcement—a common trade-off for enhanced tensile strength. At higher A-CNCs concentrations, the particle number in CTFA resin matrix also increases. The increased scattering of A-CNCs particles further inhibit the UV-light penetration during 3D printing and led to ineffective polymerization. This in-effective polymerization leads to decreases in the modulus.

Young's modulus, which reflects the stiffness of composite materials, increased significantly for the CTFA with A-CNC composite. The combination of increased tensile strength and reduced strain resulted in a highly enhanced Young's modulus, demonstrating greater stiffness (Fig. 4g). This confirms that A-CNCs are more effective at reinforcing the composite, making it stiffer and more resistant to deformation under

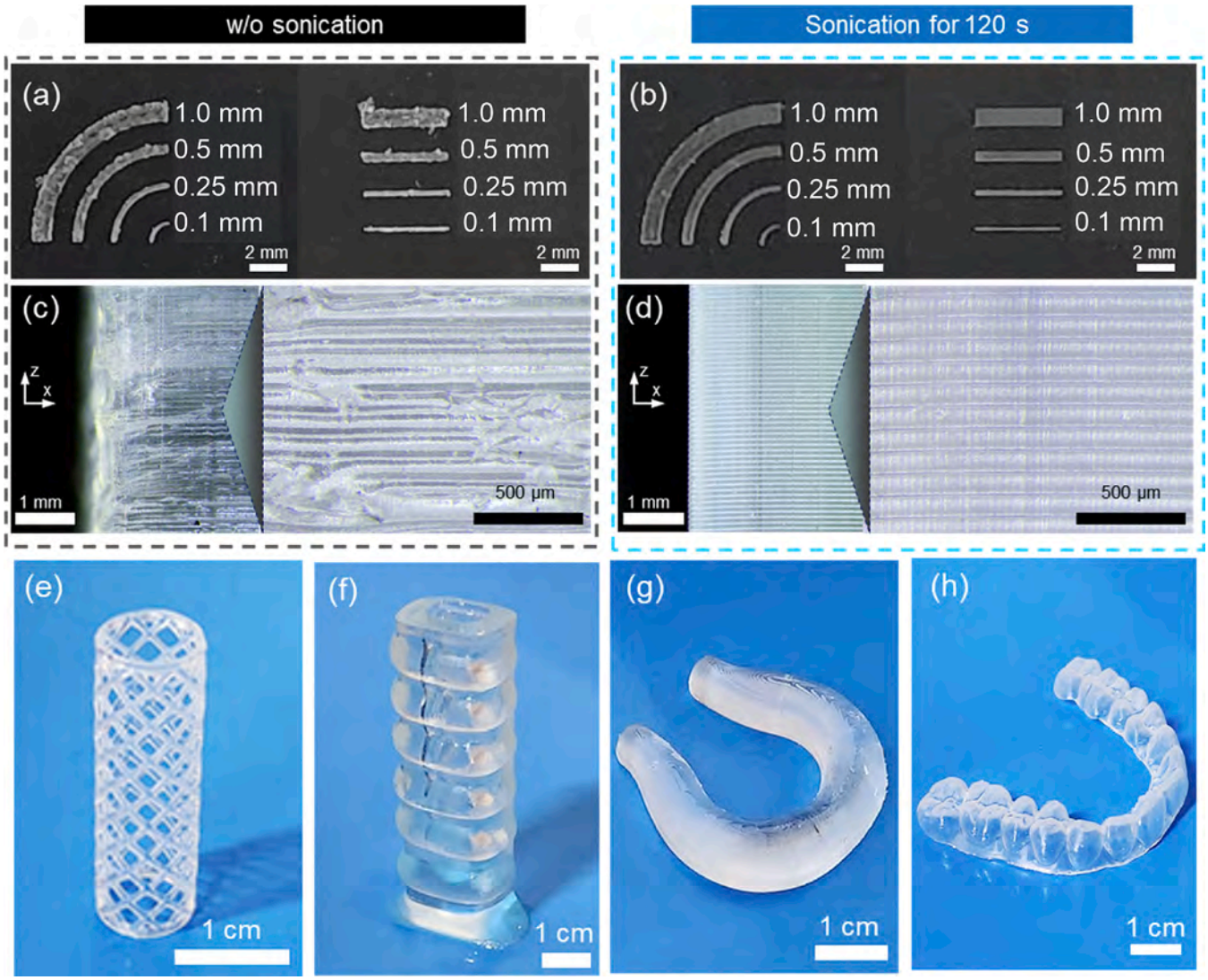

Fig. 6. Printability of the composite resin inks. Resolution of the printed concentric circles and parallel linear shapes (widths: 1.0, 0.5, 0.25, and 0.1 mm) prepared using the A-CNC/CTFA composite resin (a) without and (b) with 2 min sonication under the printing conditions of 100 μm gap and 30 s curing time. Microscopic images of the side profiles of the printed structures (c) without and (d) with 2 min sonication. 3D-printed models of the (e) cylindrical stent, (f) trachea, (g) meniscus, and (h) dental aligner.

load.

The tensile strength and modulus increased with the A-CNC content, reaching a maximum value at 0.1 wt% (Fig. 4h). The addition of A-CNCs beyond 0.1 wt% led to a decrease in the tensile strength, suggesting that the optimal dispersion of A-CNCs within the CTFA matrix occurs at 0.1 wt% (Fig. 4i). At higher A-CNC concentrations, the composite became more brittle, resulting in a reduced strain at break (Fig. 4j). The Young's modulus increased with the A-CNC content owing to the effective load-bearing capacity imparted by the well-dispersed A-CNC particles within the polymer matrix. At A-CNCs concentrations higher than 0.1 wt%, the increased particle number in the CTFA resin matrix leads to greater light scattering. This increased scattering reduces UV-light penetration during 3D printing and results in ineffective polymerization, which ultimately lowers the modulus (Fig. 4k). The observed increase in the tensile strength and modulus at 0.1 wt% A-CNCs is attributed to the optimal concentration for enhancement of mechanical properties.

The A-CNC and S-CNC CTFA composites were analyzed using Weibull statistics to calculate the Weibull modulus (which reflects the reliability of the materials) and characteristic strength (which provides an estimate of the material's lifetime). The reliability (or survival probability) of the materials at various thicknesses, based on the type and concentration of S-CNCs and A-CNCs, is shown in Fig. 4l and m, depicting specific survival probability values at 3 MPa. At 2 MPa, both materials exhibited similar reliability across all thicknesses. However, at 3 MPa, a significant difference was observed between 0.1 wt% A-CNCs and S-CNCs, with A-CNCs exhibiting substantially higher reliability than S-CNCs.

Under the condition with 0.1 wt% A-CNCs and S-CNCs added, the survival probability fitting curve shifted to the right relative to control CTFA, confirming an improvement in survival probability in Fig. 4n. The median survival stress for control CTFA was recorded at 1.849 MPa, while for 0.1 wt% A-CNCs, it was significantly higher at approximately 4.38 MPa. In contrast, the median survival stress for 0.1 wt% S-CNCs was ~2.26 MPa, emphasizing the durability difference between the two composites.

As the concentration of A-CNCs increased from 0 to 0.05 and 0.1 wt %, the survival probability in terms of tensile strength improved; however, at 0.2 wt%, the probability tended to decrease, in Fig. 4o. Overall, the durability performance comparison confirmed that the survival probability was the highest at 0.1 wt% A-CNCs, demonstrating superior mechanical reliability at this concentration.

The cytotoxicity analysis of CTFA sheets incorporated with varying

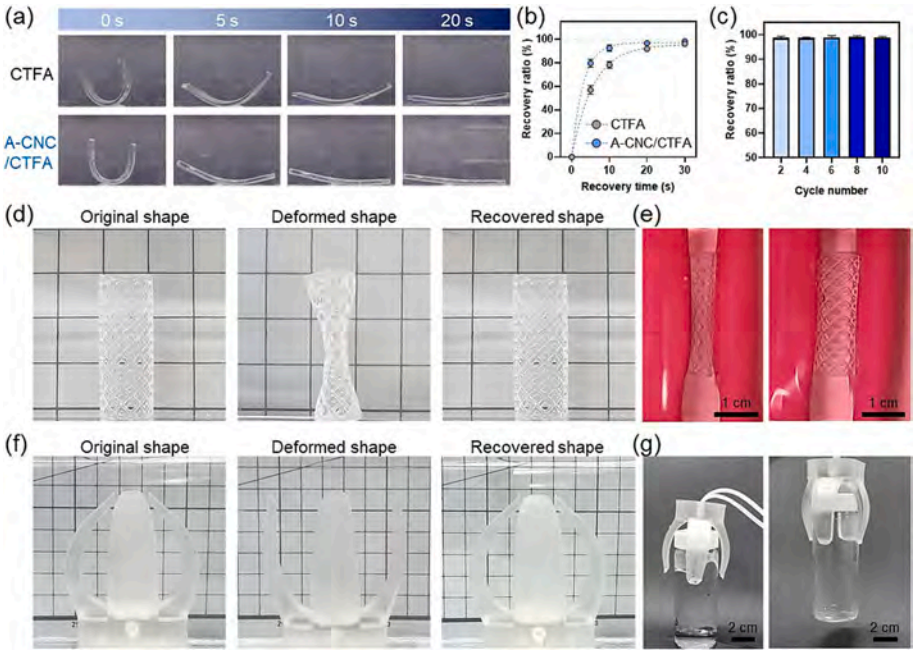

Fig. 7. Thermally induced shape memory behavior and application. (a) Shape recovery process for the CTFA and A-CNC/CTFA rectangular samples at 40 °C. (b) Recovery ratio (Rr) as a function of time for the CTFA and A-CNC/CTFA samples, illustrating the enhanced recovery performance of A-CNC/CTFA. (c) Stent model showing original, deformed, and recovered shapes. (d) Demonstration of the stent's ability to expand a constricted model blood vessel during shape recovery. (e) Gripper model showing original, deformed, and recovered shapes. (f) Functional demonstration of the gripper lifting an object.

concentrations of A-CNCs was performed using the MTT assay. It was found that the % relative metabolic activity of the NIH3T3 cells decreased slightly to 85.6 % for the sample with the CTFA sheet alone. In contrast, the CTFA sheets incorporated with 0.05 wt%, 0.1 wt%, or 0.2 wt% A-CNCs did not show any significant change in % relative metabolic activity, showing values of 84.6 %, 87.6 %, and 84.6 %, respectively (Fig. 5a). These results indicate that the incorporation of A-CNC fillers into CTFA did not negatively affect cell viability.

Additionally, the microscopic images revealed that the CTFA sheets were non-adhesive to the cells. The number of cells on the CTFA surface decreased after 1 day of seeding, and a round cell morphology was observed on the surface. In contrast, the cells on the control surface were well-spread and flattened, displaying the typical morphology of adherent cells (Figs. 5b-e). Moreover, after washing the surfaces with a fresh medium, only a few cells remained on the CTFA surface, indicating the anti-fouling characteristics of the material.

The resolution of the printed structures was influenced by the sonication process used during the preparation of the composite resin inks. Fig. 6a and b show the effects of sonication on the resolution in the x-y plane. The intended designs consisted of concentric circles and parallel linear shapes with widths of 0.1, 0.25, 0.5, and 1.0 mm. Without sonication, A-CNCs in the resin exhibited significant agglomeration, resulting in poor resolution and uneven prints. In contrast, sonication for 2 min realized high-resolution printing with clear and sharp features, indicating that the uniform dispersion of A-CNCs in the resin is essential for maintaining the high fidelity of the photocurable resin.

Fig. 6c and d present the microscopic images of the side profiles of the printed structures. The printed structures achieved by using the poorly dispersed composite resin without sonication exhibited irregular layers and uneven edges. In contrast, printed structures achieved by using the resin sonicated for 2 min had smooth and even layers with clean edges, demonstrating the effectiveness of ultrasonication in improving layer uniformity and overall printing quality.

The printability and clarity of the composite resin inks were further confirmed by printing various biomedical structural features (Fig. 6e-j). The printed structures achieved by using the appropriately sonicated resin exhibited high structural stability and were free from defects. Structures such as a cylindrical stent with uniform mesh lines, models of the trachea and meniscus, and a dental aligner demonstrated the applicability of the composite resin in biomedical engineering.

Figure 7a compares the shape recovery process of the rectangular 3D-printed samples prepared using CTFA and A-CNC/CTFA. The samples were initially deformed into a U-shape at 85 °C and then fixed in a 4 °C ice water bath to maintain the deformed shape. Subsequently, the samples were submerged in a 40 °C water bath to induce shape recovery. Figure 7b presents the shape recovery ratio (R_r) as a function of time for both CTFA and A-CNC/CTFA samples. The sequential images and shape recovery ratios demonstrate that the A-CNC/CTFA sample recovers its original shape at a higher rate compared to the control CTFA sample, highlighting its superior shape memory performance. This enhanced recovery speed is attributed to the increased modulus of the printed material with the addition of A-CNCs, as shown in the previous mechanical property analysis. A higher modulus indicates a stronger ability to maintain the original state of the polymer, resulting in a faster recovery process. Figure 7c illustrates the recovery ratio after 30 s for each cycle over ten repeated shape recovery cycles. The shape memory behavior of the A-CNC/CTFA sample remained consistent even after multiple cycles, with the original shape fully recovered within 30 s during each cycle. This indicates that the 3D printed A-CNC/CTFA has stable shape memory performance with consistent recovery ratio and speed and is suitable for repetitive use.

Fig. 7d shows the shape memory performance of a stent model, demonstrating its original, deformed, and recovered shapes. The stent nearly returns to its original shape upon exposure to the recovery conditions, illustrating the material's potential in biomedical applications where precise shape restoration is critical. Fig. 7e provides a visual demonstration of the stent's application within a model blood vessel. As the stent recovers its original shape, it effectively expands the constricted section of the vessel, showcasing the potential of this material for use in minimally invasive medical procedures such as angioplasty.

Fig. 7f displays the original, deformed, and recovered shapes of a 3D-printed gripper. Similar to the stent model, the gripper nearly achieves its original shape. Fig. 7g illustrates the functional performance of the gripper model. The gripper could successfully lift an object weighing

over 170 g, demonstrating not only its shape recovery ability but also its practical utility in applications requiring mechanical gripping and manipulation.

4. Conclusions

This study demonstrated the enhanced properties of 3D printing materials using a composite of CTFA and CNCs. In particular, the integration of A-CNCs significantly improved the optical clarity and mechanical performance of the composite ink. Through ultrasonication, A-CNCs were uniformly dispersed within the resin matrix, leading to enhanced printing precision and increased mechanical strength.

The mechanical strength of the composite resin containing A-CNCs was significantly greater than that of containing S-CNCs, with the maximum performance enhancement achieved at an optimal concentration of 0.1 wt%. At this concentration, both tensile strength and Young's modulus were considerably improved because A-CNCs more effectively transferred and distributed load within the resin. This resulted in stronger physical interactions within the composite material, while maintaining high transparency and superior mechanical properties.

Moreover, the composite containing A-CNCs exhibited thermally induced shape memory properties, demonstrating fast recovery and high physical stability. This demonstrates the potential of the A-CNC-based composite in high-precision biomedical applications such as development of medical devices. The results of this study emphasize the crucial role of physical and chemical manipulation of nanomaterials in enhancing the performance of 3D printing materials, particularly for applications requiring high performance and biocompatibility.

The incorporation of A-CNCs achieved a significantly greater mechanical reinforcement than that of S-CNCs, contributing to improved printing precision and structural stability of the composite ink. These findings indicate that A-CNCs have great potential in 3D printing applications wherein high strength and precision are required, particularly the production of medical devices.

CRediT authorship contribution statement

Junsik Choi: Writing – original draft, Funding acquisition, Data curation, Conceptualization. **Deepika Thakur:** Visualization, Investigation, Formal analysis. **Jinhong Min:** Resources, Methodology, Data curation. **Jiho Lee:** Visualization, Methodology. **Hoon Kim:** Writing – review & editing, Supervision, Project administration, Formal analysis. **Jinho Hyun:** Writing – review & editing, Validation, Supervision.

Declaration of competing interest

The authors declare that they have no known competing financial interests or personal relationships that could have appeared to influence the work reported in this paper.

Acknowledgements

J.C. and D.T. contributed equally to this work. This paper was supported by Korea Evaluation Institute of Industrial Technology (KEIT) grant funded by the Korea Government (MOTIE) (20023781-K_G012002378102-10054408). This work was supported by the National Research Foundation of Korea (NRF) grant funded by the Korea government (MSIT) (RS-2024-00352624).

References

[1] Herbert R, Lim HR, Park S, Kim JH, Yeo WH. Recent advances in printing technologies of nanomaterials for implantable wireless systems in health monitoring and diagnosis. Adv Healthc Mater 2021;10:e2100158. https://doi.org/10.1002/adhm.202100158.

[2] Sultan S, Siqueira G, Zimmermann T, Mathew AP. 3D printing of nano-cellulosic biomaterials for medical applications. Current Opinion in Biomedical Engineering 2017;2:29–34. https://doi.org/10.1016/j.cobme.2017.06.002.

[3] Kong YL, Gupta MK, Johnson BN, Mcalpine MC. 3D printed bionic nanodevices. Nano Today 2016;11:330–50. https://doi.org/10.1016/j.nantod.2016.04.007.

[4] Murphy SV, Atala A. 3D bioprinting of tissues and organs. Nat Biotechnol 2014;32:773–85. https://doi.org/10.1038/nbt.2958.

[5] Norman J, Madurawe RD, Moore CMV, Khan MA, Khairuzzaman A. A new chapter in pharmaceutical manufacturing: 3D-printed drug products. Adv Drug Deliv Rev 2017;108:39–50. https://doi.org/10.1016/j.addr.2016.03.001.

[6] Liu M, Zhang Q, Zhao Y, Liu C, Shao Y, Tong X. A high sensitivity micro-pressure sensor based on 3D printing and screen-printing technologies. Meas Sci Technol 2020:31. https://doi.org/10.1088/1361-6501/ab5749.

[7] Schupp W, et al. Shape memory aligners: a new dimension in aligner orthodontics. J Aligner Orthod 2023:7.

[8] Tartaglia GM, Mapelli A, Maspero C, Santaniello T, Serafin M, Farronato M, et al. Direct 3D printing of clear orthodontic aligners: current state and future possibilities. Materials 2021:14. https://doi.org/10.3390/ma14071799.

[9] Guvendiren M, Molde J, Soares RMD, Kohn J. Designing biomaterials for 3D printing. ACS Biomater Sci Eng 2016;2:1679–93. https://doi.org/10.1021/acsbiomaterials.6b00121.

[10] Lee SY, Kim H, Kim HJ, Chung CJ, Choi YJ, Kim SJ, et al. Thermo-mechanical properties of 3D printed photocurable shape memory resin for clear aligners. Sci Rep 2022;12:6246. https://doi.org/10.1038/s41598-022-09831-4.

[11] Lee J, Kim H, Kim H, Lee T, Kim JH, Andreu A, et al. Average-accumulated normalized dose (A-AND) predicts ultimate tensile strength and elastic modulus of photopolymer printed by vat photopolymerization. Addit Manuf 2022:55. https://doi.org/10.1016/j.addma.2022.102799.

[12] Li Y, Mao Q, Yin J, Wang Y, Fu J, Huang Y. Theoretical prediction and experimental validation of the digital light processing (DLP) working curve for photocurable materials. Addit Manuf 2021:37. https://doi.org/10.1016/j.addma.2020.101716.

[13] Chen Q, Mangadlao JD, Wallat J, De Leon A, Pokorski JK, Advincula RC. 3D printing biocompatible polyurethane/poly(lactic acid)/graphene oxide nanocomposites: anisotropic properties. ACS Appl Mater Interfaces 2017;9:4015–23. https://doi.org/10.1021/acsami.6b11793.

[14] Chen L, Shao L, Wang F, Huang Y, Gao F. Enhancement in sustained release of antimicrobial peptide and BMP-2 from degradable three dimensional-printed PLGA scaffold for bone regeneration. RSC Adv 2019;9:10494–507. https://doi.org/10.1039/c8ra08788a.

[15] Dubey N, Ferreira JA, Malda J, Bhaduri SB, Bottino MC. Extracellular matrix/amorphous magnesium phosphate bioink for 3D bioprinting of craniomaxillofacial bone tissue. ACS Appl Mater Interfaces 2020;12:23752–63. https://doi.org/10.1021/acsami.0c05311.

[16] Han L, Xu J, Lu X, Gan D, Wang Z, Wang K, et al. Biohybrid methacrylated gelatin/polyacrylamide hydrogels for cartilage repair. J Mater Chem B 2017;5:731–41. https://doi.org/10.1039/c6tb02348g.

[17] Yang S, Chen T, Bu Z, Tuo X, Gong Y, Guo J. Thermal responsive photopolymerization 3D printed shape memory polymers enhanced by heat transfer media. J Appl Polym Sci 2023:140. https://doi.org/10.1002/app.53514.

[18] Kim H, Kim J, Ryu KH, Lee J, Kim HJ, Hyun J, et al. Embedded direct ink writing 3D printing of UV curable resin/sepiolite composites with nano orientation. ACS Omega 2023;8:23554–65. https://doi.org/10.1021/acsomega.3c01165.

[19] Markstedt K, Escalante A, Toriz G, Gatenholm P. Biomimetic inks based on cellulose nanofibrils and cross-linkable xylans for 3D printing. ACS Appl Mater Interfaces 2017;9:40878–86. https://doi.org/10.1021/acsami.7b13400.

[20] Kim H, Ryu KH, Baek D, Khan TA, Kim HJ, Shin S, et al. 3D printing of polyethylene terephthalate glycol-sepiolite composites with nanoscale orientation. ACS Appl Mater Interfaces 2020;12:23453–63. https://doi.org/10.1021/acsami.0c03830.

[21] Wu C, Mangal U, Seo JY, Kim H, Bai N, Cha JY, et al. Enhancing biofilm resistance and preserving optical translucency of 3D printed clear aligners through carboxybetaine-copolymer surface treatment. Dent Mater 2024;40:1575–83. https://doi.org/10.1016/j.dental.2024.07.009.

[22] Mali P, Sherje AP. Cellulose nanocrystals: fundamentals and biomedical applications. Carbohydr Polym 2022;275:118668. https://doi.org/10.1016/j.carbpol.2021.118668.

[23] Hausmann MK, Rühs PA, Siqueira G, Läuger J, Libanori R, Zimmermann T, et al. Dynamics of cellulose nanocrystal alignment during 3D printing. ACS Nano 2018;12:6926–37. https://doi.org/10.1021/acsnano.8b02366.

[24] Zhang S, Huang D, Lin H, Xiao Y, Zhang X. Cellulose nanocrystal reinforced collagen-based nanocomposite hydrogel with self-healing and stress-relaxation properties for cell delivery. Biomacromolecules 2020;21:2400–8. https://doi.org/10.1021/acs.biomac.0c00345.

[25] Weng Z, Zhou Y, Lin W, Senthil T, Wu L. Structure-property relationship of nano enhanced stereolithography resin for desktop SLA 3D printer. Compos A 2016;88:234–42. https://doi.org/10.1016/j.compositesa.2016.05.035.

[26] Wang Q, Liu X, Qiang Z, Hu Z, Cui X, Wei H, et al. Cellulose nanocrystal enhanced, high dielectric 3D printing composite resin for energy applications. Compos Sci Technol 2022;227:109601. https://doi.org/10.1016/j.compscitech.2022.109601.

[27] Feng X, Wu Z, Xie Y, Wang S. Reinforcing 3D print methacrylate resin/cellulose nanocrystal composites: effect of cellulose nanocrystal modification. BioResources 2019;14:3701–16. https://doi.org/10.15376/biores.14.2.3701-3716.
[28] Li VCF, Kuang X, Mulyadi A, Hamel CM, Deng Y, Qi HJ. 3D printed cellulose nanocrystal composites through digital light processing. Cellulose 2019;26: 3973–85. https://doi.org/10.1007/s10570-019-02353-9.
[29] Kedzior SA, Graham L, Moorlag C, Dooley BM, Cranston ED. Poly(methyl methacrylate)-grafted cellulose nanocrystals: one-step synthesis, nanocomposite preparation, and characterization. Can J Chem Eng 2016;94:811–22. https://doi.org/10.1002/cjce.22456.